*Article*

# Sponge-like CoNi Catalysts Synthesized by Combustion of Reactive Solutions: Stability and Performance for CO₂ Hydrogenation

**Nikolay Evdokimenko** [1,2], **Zhanna Yermekova** [1], **Sergey Roslyakov** [1,*], **Olga Tkachenko** [2], **Gennady Kapustin** [2], **Denis Bindiug** [1], **Alexander Kustov** [1,2,3] **and Alexander S. Mukasyan** [4,*]

1 Center of Functional Nano-Ceramics, National University of Science and Technology "MISiS", 119049 Moscow, Russia; nikolayevdokimenko@bk.ru (N.E.); ifjanna@gmail.com (Z.Y.); denis-bindyug@yandex.ru (D.B.); kyst@list.ru (A.K.)
2 N.D. Zelinsky Institute of Organic Chemistry RAS, 119991 Moscow, Russia; ot113@mail.ru (O.T.); gik@server.ioc.ac.ru (G.K.)
3 Department of Chemistry, M. V. Lomonosov Moscow State University, 119991 Moscow, Russia
4 Department of Chemical and Biomolecular Engineering, University of Notre Dame, Notre Dame, IN 46556, USA
* Correspondence: roslyakov.si@misis.ru (S.R.); amoukasi@nd.edu (A.S.M.)

**Abstract:** Active and stable catalysts are essential for effective hydrogenation of gaseous CO₂ into valuable chemicals. This work focuses on the structural and catalytic features of single metals, i.e., Co and Ni, as well as bimetallic CoNi alloy catalysts synthesized via combustion of reactive sol-gels. Different characterization methods were used for studying the relationships between the structure, composition, and catalytic activity of the fabricated materials. All catalysts exhibited highly porous sponge-like microstructure. The outermost surfaces of the CoNi alloys were more saturated with Co, while a stoichiometric Co/Ni ratio was observed for the particle's bulk. Catalytic properties of the as-synthesized powders were studied in the CO₂ hydrogenation reaction at 300 °C for over 80 h of time on stream. All the catalysts demonstrated exceptional selectivity with respect to CH₄ formation. However, the combination of elemental Co and Ni in a single phase resulted in a synergistic effect in bulk alloy catalysts, with activity twofold to threefold that of single-metal catalysts. The activity and stability of the CoNi₃ catalyst were higher than those previously reported for Ni-based catalysts. The reasons for this behavior are discussed.

**Keywords:** combustion; CoNi alloys; catalysis; CO₂ hydrogenation; methanation

## 1. Introduction

Reducing CO₂ emission into the atmosphere is a critical, climate-defining issue that has been a topic of significant interest during the last decade [1–3]. Conversion of CO₂ into synthetic natural gas (syngas) through its catalytic hydrogenation (Equation (1)) is considered promising for the recycling of captured or newly produced CO₂, although many other valuable chemicals could also be produced using this approach [4–7].

$$CO_2 + 4H_2 \rightleftharpoons CH_4 + 2H_2O, \Delta H_{298}K = -165.0 \text{ kJ/mol} \tag{1}$$
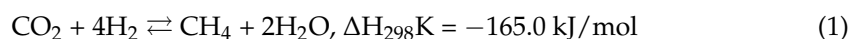
Noble and rare-earth metal-based catalysts are known for their high efficiency with respect to CO₂ hydrogenation, but the growing demand for these catalysts has prompted the search for more commercially appealing materials [8,9]. Transition metals have attracted significant attention as cost-efficient alternatives [10]. Among these, Ni exhibits exceptional selectivity for the conversion of CO₂ into CH₄, but has some drawbacks, such as the relatively low lifetime of the catalysts owing to the sintering, oxidation, and carbonization of the metal active sites [11].

The specific interaction of metal particles with the supporting material is a viable approach for stabilizing active Ni sites against sintering and oxidation. The effect of the supporting material on the Ni catalyst modification has been intensely studied for single-phase substrates such as $Al_2O_3$ [12,13], $TiO_2$ [14,15], $SiO_2$ [16–18] $CeO_2$ [12,19,20], $ZrO_2$ [12,21], and hybrid materials with or without additional catalytically active dopants [22–27]. In all cases, however, there is a significant difference between the thermal conductivities of Ni (90.7 W/m·K) and ceramic supports (e.g., that of $CeO_2$, at 8 W/m·K [28]), which often leads to the formation of local hot spots and subsequent carbonization of active sites [11,29].

The catalyst properties can be improved by controlling the catalyst composition, using, for example, bimetallic phases [30–32]. Specifically, Co has been a promising additive for modifying the electronic and crystal structures of Ni. For example, it was reported that the formation of a homogeneous Ni-Co alloy led to good CO conversion and $CH_4$ selectivity at temperatures below 380 °C [29]. The electron enrichment of the Ni-Co alloy contributed to the $CO_2$ adsorption, CO dissociation, and $H_2$ spillover, which facilitated $CH_4$ formation and the removal of deposited C species.

Recently, increasing attention has been paid to the development of structural catalysts, with the catalysts' surface texture [33,34] and morphology as the key parameters for improving their performance and stability [35–38]. Sponge-like structured catalysts are highly advantageous, owing to their high surface-to-volume ratio and good mass and heat transfer at low-pressure drops [8,39,40]. The implementation of transition-metal foams in the $CO_2$ hydrogenation reaction may significantly improve the heat transfer from the overheated spots through the thin walls of the sponge framework, thereby increasing the catalyst stability [41].

Sol-gel combustion synthesis (SGCS) is a unique approach for tailoring the morphology of a material, and allows the fabrication of metallic foams with controlled pore-size distribution [42–45]. In this work, we studied the synergetic effect of Co-Ni bonds in bulk Co-Ni alloys on the $CO_2$ conversion reaction run on sponge-like structural metal catalysts fabricated by SGCS. Different $Co_xNi_{1-x}$ compositions were synthesized, with x parameter values of 1, 0.75, 0.5, 0.25, and 0. The relationships between the structure, composition, and catalytic performance of the materials for $CO_2$ hydrogenation were investigated at 300 °C for up to 80 h of time on stream (TOS).

## 2. Materials and Methods

### 2.1. Preparation of Catalysts

The catalysts were synthesized via the SGCS of a reactive mixture of metal nitrates and organic fuels [45]. Specifically, $Co(NO_3)_2·6H_2O$ and $Ni(NO_3)_2·6H_2O$ nitrates were used as metal-containing sources/oxidizers for fabricating single-metal (Ni or Co) and bimetallic ($CoNi_3$, CoNi, and $Co_3Ni$) materials. Aminoacetic acid ($C_2H_5NO_2$) was used as a structure-forming reducer/fuel. All chemicals (Chimmed, Moscow, Russia) were 98% purity grade. The fuel-to-oxidizer molar ratio, φ, was kept equal to 1.5 for all mixtures. It is worth noting that this ratio was selected based on our previous work [46] and allowed both the self-propagating reaction mode and the formation of pure metallic phases. For each reactive mixture, the metal nitrates were dissolved in 80 mL of distilled water, following which the corresponding amount of fuel was added. The obtained aqueous solution was mixed thoroughly for 30 min using a magnetic stirrer, until a homogeneous mixture was formed. Each reactive solution was kept in a furnace at 80 °C for 24 h to form a gel-like medium. The SGCS performed in an inert atmosphere of Ar inside a stainless-steel chemical reactor [45]. The combustion reaction was triggered using a resistively heated tungsten wire. After the local preheating of the reactive gel, the initiated combustion front propagated along the reactive medium in the self-sustained mode. In the combustion wave, the gel was converted into a solid product, which was investigated using various material characterization techniques.

### 2.2. Structural Characterization

The phase compositions of the powders were studied using X-ray diffraction (XRD). The XRD analysis was performed at room temperature using a DIFREY-401 diffractometer, operated at 25 kV and 40 mA using a Cu-Kα radiation source with a Bragg–Brentano focusing geometry. A JSM 7600F (JEOL, Akishima, Japan) field emission scanning electron microscope with a spatial resolution of ~1 nm, equipped with an elemental microanalysis system (EDX, Oxford Instruments, Abingdon-on-Thames, UK), was used for studying the product morphology and elemental ratios in the samples. XPS analysis was performed on an Axis Ultra DLD (Kratos Analytical, Manchester, UK) instrument with an Al-*K*α radiation source operating at 1456.6 eV. The binding energy of C1s (285 eV) was used as the internal standard. All spectra were recorded in the 20–1460 eV range. C 1s, Ni 2p, Co 2p, O 1s, and N 1s were recorded with 0.1 eV step sizes. The elemental composition of the catalysts was acquired in the outermost layer (thickness, 5–10 nm), and the atomic ratio of the elements was calculated from the integral line intensity corrected by the Scofield photoionization cross-section.

### 2.3. Performance Evaluation

The as-prepared bulk catalysts were studied for $CO_2$ hydrogenation at a pressure of 2 MPa and temperature of 300 °C. A mixture of as-synthesized catalytically active metal particles, with diameters in the 50–100 μm range, and a quartz buffer powder (size, 100–500 μm) was prepared. Specifically, 0.2 g of the metallic catalyst was mixed with 0.8 g of quartz powder. To preserve the sponge-like structure of the catalysts, the mixture was not subjected to any additional mechanical treatment. Thus, the prepared mixture was loaded into a continuous-flow stainless-steel fixed-bed reactor (inner diameter, 4 mm). Before the catalytic reaction, each sample was reduced under the following conditions: temperature, 300 °C; heating rate, 10 °C/min; $H_2$ flow rate, 50 mL/min; and run time, 1 h. After the catalyst activation, the feed gas was switched to a mixture of $CO_2$ and $H_2$ with a volume ratio of 1:4 and gas flow rates in the 3–12 mL/min range. Thus, the total volumetric flow rate of the initial mixture was 15 mL/min, while the volumetric hourly space velocity (VHSV) was 4500 mL $g^{-1}h^{-1}$. Before the actual measurements, each sample was kept under the above conditions for 2 h for reaching thermodynamic equilibrium.

Analysis of the reaction products was performed using a KRISTALL 5000 chromatograph equipped with three heat capacity detectors, one flame ionization detector, and three columns: M NaX 80/100 mesh 2 m/2 mm, HayeSep R 80/100 mesh 1 m/2 mm, and HayeSep Q 80/100 mesh 1 m/2 m, and with a capillary column MXT®-Alumina BOND/MAPD 30 m/0.53 mm.

The $CO_2$ gas conversion was calculated as:

$$K_{CO_2} = 100\% \frac{\left(G_s X^0_{CO_2} - G_f X_{CO_2}\right)}{G_s X^0_{CO_2}} \tag{2}$$

where $G_s$ is the gas mixture flow (L/h) at the reactor inlet, $G_f$ is the gas mixture flow (L/h) at the reactor outlet, $X^0_{CO_2}$ is the $CO_2$ fraction before the catalytic reaction, and $X_{CO_2}$ is the $CO_2$ fraction after the catalysis.

Productivity of the $CO_2$ hydrogenation was calculated as follows:

$$r = \frac{\left(n(CO_2)_s - n\left(CO_2\right)_f\right)}{m_{cat}} \tag{3}$$

where $n(CO_2)_s$ is the inlet molar flow rate of $CO_2$ (mol/h), $n(CO_2)_f$ is the outlet molar flow rate of $CO_2$ (mol/h), and $m_{cat}$ is the total mass (kg) of the loaded catalyst.

The product formation selectivity without considering water formation was calculated as follows:

$$S_i = \frac{Y_i}{\sum Y_i} \tag{4}$$

where $Y_i$ is the portion of the $i$th reaction product in the final flow after the catalytic hydrogenation process, while $S_{CO} + S_{HC} = 100\%$, where $S_{CO}$ is the CO selectivity and $S_{HC}$ is the $C_1–C_4$ formation selectivity.

The $CH_4$ fraction ($f_{CH_4}$) from the total amount of product was calculated as follows:

$$f_{CH_4} = S_{CH_4}/S_{HC} \tag{5}$$

*2.4. In Situ Diffuse Reflectance Infrared Fourier Transform Spectroscopy (DRIFTS) Experiments*

In situ DRIFTS experiments were performed using an FTIR spectrometer (NICOLET "Protege" 460) equipped with a homemade diffuse reflectance attachment [47]. IR spectra were recorded in the 6000–400 cm$^{-1}$ range at a resolution of 4 cm$^{-1}$. To regulate the signal-to-noise ratio, 500 spectra were processed. Prior to the measurements, all of the samples were subjected to thermo-vacuum treatment at 300 °C (heating rate, 5 °C/min) and P = 0.13 Pa, for 2 h. The CO and $CO_2$ adsorption occurred at room temperature (27 °C) in the P = 2.1–3 kPa and P = 1.3–2.4 kPa ranges, respectively. The absorption band intensity was measured according to the Kubelka–Munk theory. $CaF_2$ powder was used as the reference material. Registration and spectral processing were performed using the OMNIC software. The CO and $CO_2$ absorption spectra are shown as the differences between the data before and after adsorption. The 2338 cm$^{-1}$ frequency shift of the $\nu_3$ $CO_2$ absorption band with respect to the value in the free state was used as a standard [48].

*2.5. Temperature-Programmed Reduction Experiments*

$H_2$-TPR measurements were performed using a semi-automatic setup with a thermal-conductivity detector. The specimen (mass, 100–150 mg) was placed in a quartz U-shaped reactor with a type-K thermocouple placed at the center of the sample. The sample was preliminarily outgassed under an Ar (30 mL/min) flow at 300 °C for 30 min, at a 10 °/min heating rate. Then, the sample was cooled to room temperature, and the feed gas was changed to a 5% $H_2$/Ar mixture. After the stabilization of the baseline, the sample was heated to 850 °C, at a 10 °C/min heating rate. The water byproduct was removed by the trap placed between the reactor and the detector and cooled to −100 °C by a mixture of liquid N and ethanol. The katharometer signal and temperature were recorded on a computer using an analog-to-digital converter and Ekochrome software package. The detector was calibrated using CuO reduction (Aldrich-Chemie GmbH, 99%, St. Louis, MO, USA). All of the results were normalized to 1 g of the sample.

### 3. Results

*3.1. Structural Characterization*

The results of the XRD analysis of the SGCS catalysts are presented in Figure 1 and Table 1. According to the XRD data, the samples consisted of a single-metal phase (Co or Ni), or bimetallic $Co_xNi_{1-x}$ phases (for x = 0.25, 0.5, 0.75), all with a face-centered-cubic (FCC) crystal structure (Fm-3m space group). The positions of the main peaks for the $Co_3Ni$ (44.349°), CoNi (44.365°), and $CoNi_3$ (44.486°) samples were shifted to a range between the peaks of the constituent elements of Co (44.206°) and Ni (44.502°), which correspond to the JCPDS data for Co (PDF#15-0806) and Ni (PDF#04-0850). The observed changes in the peak positions of the bimetallic phases depending on the concentrations of Co and Ni agreed well with Vegard's law and indicated the formation of disordered substitutional solid solutions ($Co_xNi_{1-x}$) for a range of lattice parameters (Table 1) [49]. The XRD data indicated that no other crystalline phases, except for the desired stoichiometric composition, were formed. The crystallite size (D) for each material, calculated using the Scherrer equation, was in the 27–40 nm range, indicating a high degree of crystallinity.
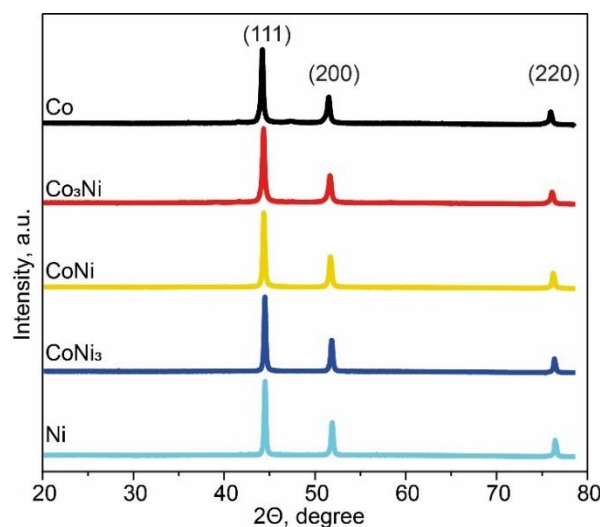
**Figure 1.** XRD patterns of the catalyst powders synthesized by SGCS.

**Table 1.** Structure characteristics of the catalysts.

| Sample ID | Crystallite Size (D), nm | Lettice Constant (a), Å |
| --- | --- | --- |
| Co | 29 | 3.5457 |
| $Co_3Ni$ | 27 | 3.5349 |
| CoNi | 32 | 3.5336 |
| $CoNi_3$ | 37 | 3.5246 |
| Ni | 38 | 3.5233 |

The typical morphologies of the SGCS catalysts are shown in Figure 2. These materials are characterized by a highly porous microstructure, which generally resembles sponge-like agglomerations. The surfaces of the agglomerates depended on the catalyst composition and exhibited some unique patterns. Each material had cavities with a specific wall shape that had a visible number of open pores.

In the case of the Co catalyst (Figure 2a), the cavities pierced the body of the sample. Within the same particle, two types of pores were observed: larger pores (1–3 μm) and smaller submicrometer-scale pores (~300 nm). High-magnification images revealed that the walls featured many small pores with no strict underlying pattern, with the pores' sizes in the 100–200 nm range. Following the addition of 25 at. % of Ni to Co (yielding the formation of the $Co_3Ni$ structure), the alloy's microstructure completely lost the Co-specific surface pattern, with all of the cavities shrunk (Figure 2b). The alloy consisted of nanometerscale (~30 nm) crystals that agglomerated in large slices, with a relatively small number of pores. There was an empty space between the slices, where Co-like microstructures with large cavities elongated in one direction were present. For the equiatomic (CoNi) composition (Figure 2c), the microstructure of the particles resembled that of Co; however, it featured thicker walls and larger pores. When the amount of Co in the alloy was 25 at. % ($Ni_3Co$), the microstructure of the agglomerates changed again, from a mono-carcass sponge to the one consisting of bridges, each of which with its own cavities and pores (Figure 2d). Moreover, small inclusions of nanoparticles could be distinguished over the entire bridge surface. At this point, the structure resembled the Ni microstructure consisting of thick bridges, chaotically interconnected with each other (Figure 2e). A closer examination revealed that the wall thickness of the Ni sponge was on the scale of a few micrometers, the surface was smooth in the middle and had many small outgrowth chips at the edges.

It is worth noting that in the case of supported catalysts, the structural porosity and specific surface area are primarily defined by the supporting material and do not depend much on the Co/Ni ratio [30,50–52]. In the case of SGCS-alloy catalysts, the structure is

defined by catalytically active constituents, where the addition of Co to the Ni base leads to a visible increase in the porosity of the bulk alloys.
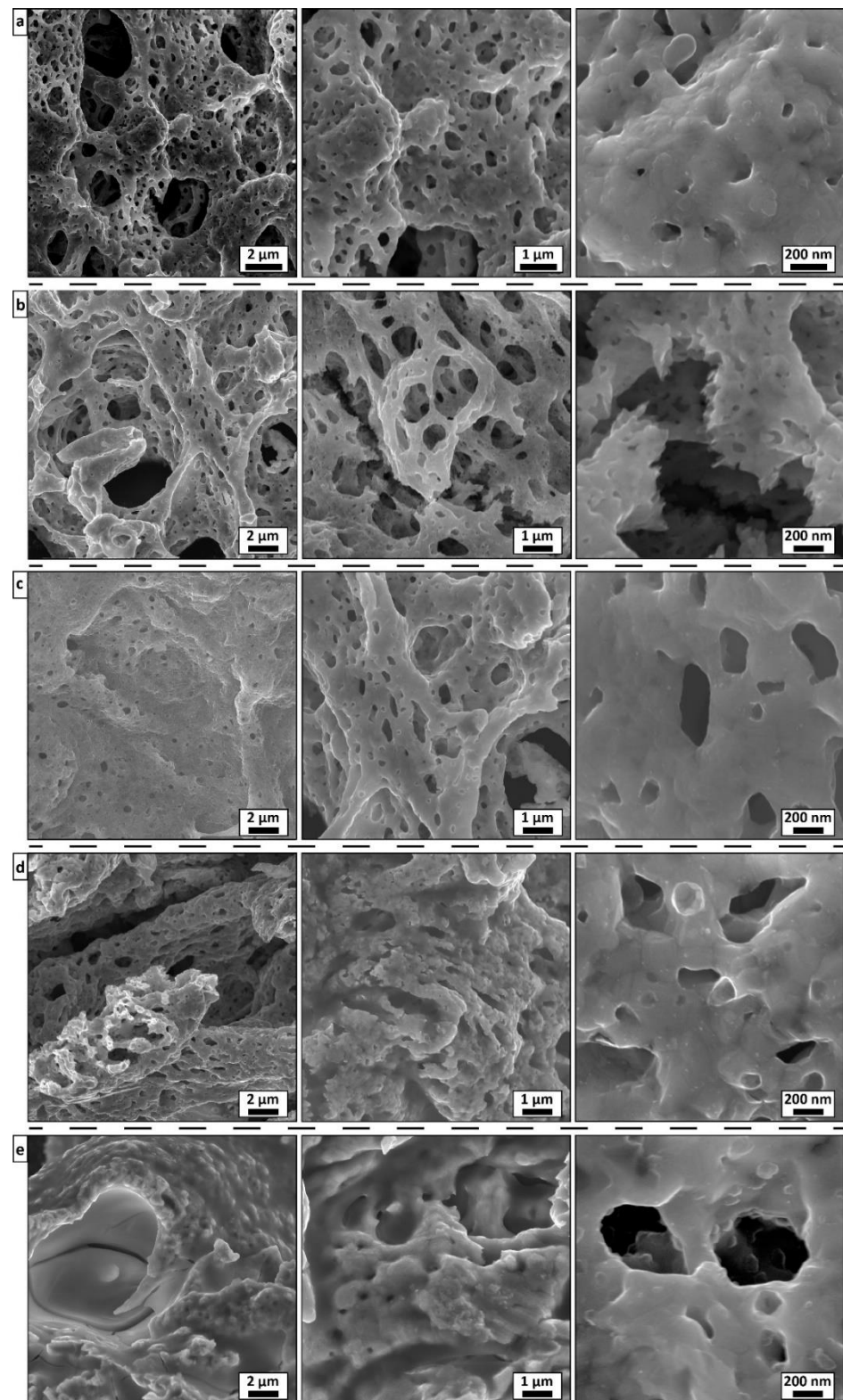


**Figure 2.** SEM images of (**a**) Co, (**b**) Co$_3$Ni, (**c**) CoNi, (**d**) CoNi$_3$, and (**e**) Ni bulk catalyst powders synthesized by SGCS.

XPS investigations of the SGCS powders were performed for analyzing the chemical composition and binding states of the elements on the outermost surfaces of the catalysts. Table S1 shows the results of the XPS survey spectra calculated as the average elemental content on the surface of the catalysts. According to the data, the outermost surfaces of all the synthesized catalysts contained contaminants such as C, O, and N. The C, O, and N contents were in the 47–59 at. % range, 19–32 at. % range, and 7–15 at. % range, respectively. These elements were the decomposition products of the initial precursors and could be readily removed by short-term heat treatment [46].

More importantly, the Co/Ni ratio in the near-surface layers (5–10 nm, analyzed by XPS) of the bimetallic catalysts appeared to be higher, compared with the stoichiometric composition (i.e., 5.2 vs. 3.0; 1.9 vs. 1.0; and 0.8 vs. 0.33, for $Co_3Ni$, CoNi, and $CoNi_3$ alloys, respectively). However, the ratios measured by EDS diagnostics (average from the volume on a scale of ~2 μm) agreed well with expected stoichiometry results (Figure S1).

The Co and Ni binding states within the near-surface region of the as-synthesized catalysts were studied by analyzing high-resolution XPS spectra of the Co 2p and Ni 2p energy levels (Figure 3). The Co 2p and Ni 2p spectra of all the samples were fitted into two main binding-energy signals of Co $2_{3/2}$, Co $2p_{1/2}$, and Ni $2p_{3/2}$, Ni $2p_{1/2}$, respectively. The former two signals were assigned to the core levels of Co(III) and Co(II), while the latter was associated with the Ni(II) oxidative state. Low-intensity metallic peaks in the Co(0) and Ni(0) states were also observed for all the investigated catalysts. Recall that the XRD analysis revealed only metallic phases.
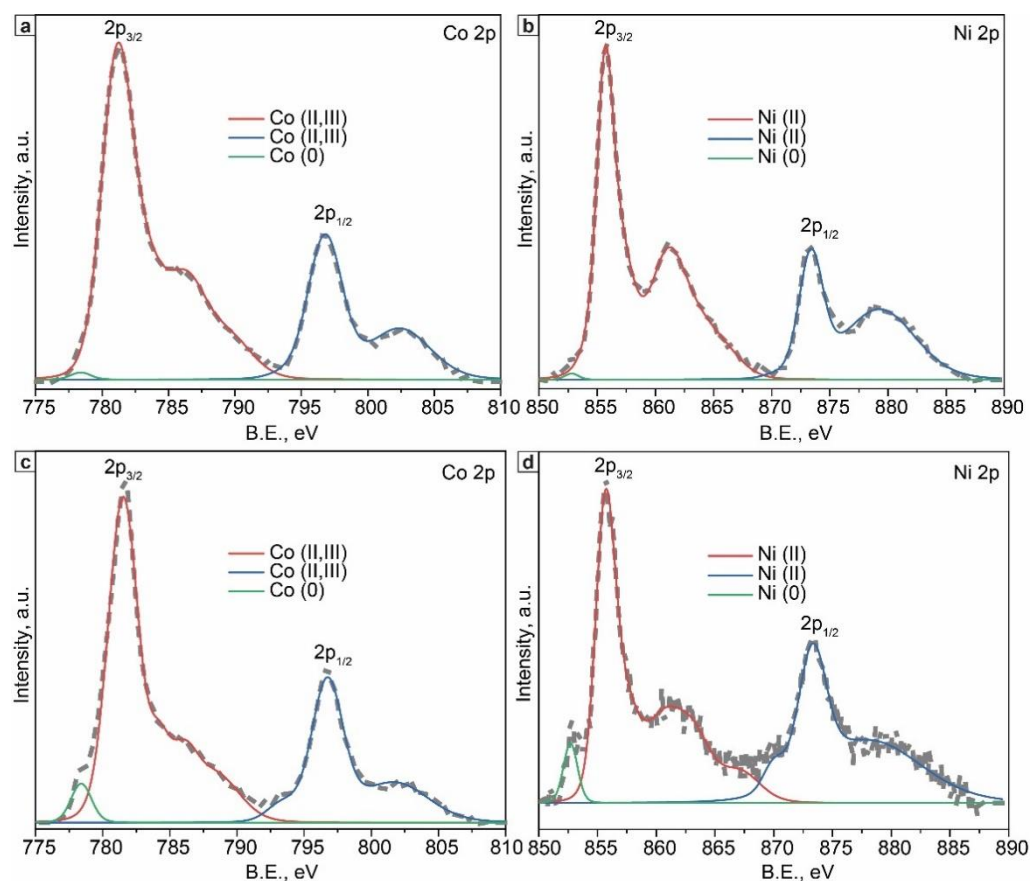


**Figure 3.** *Cont.*
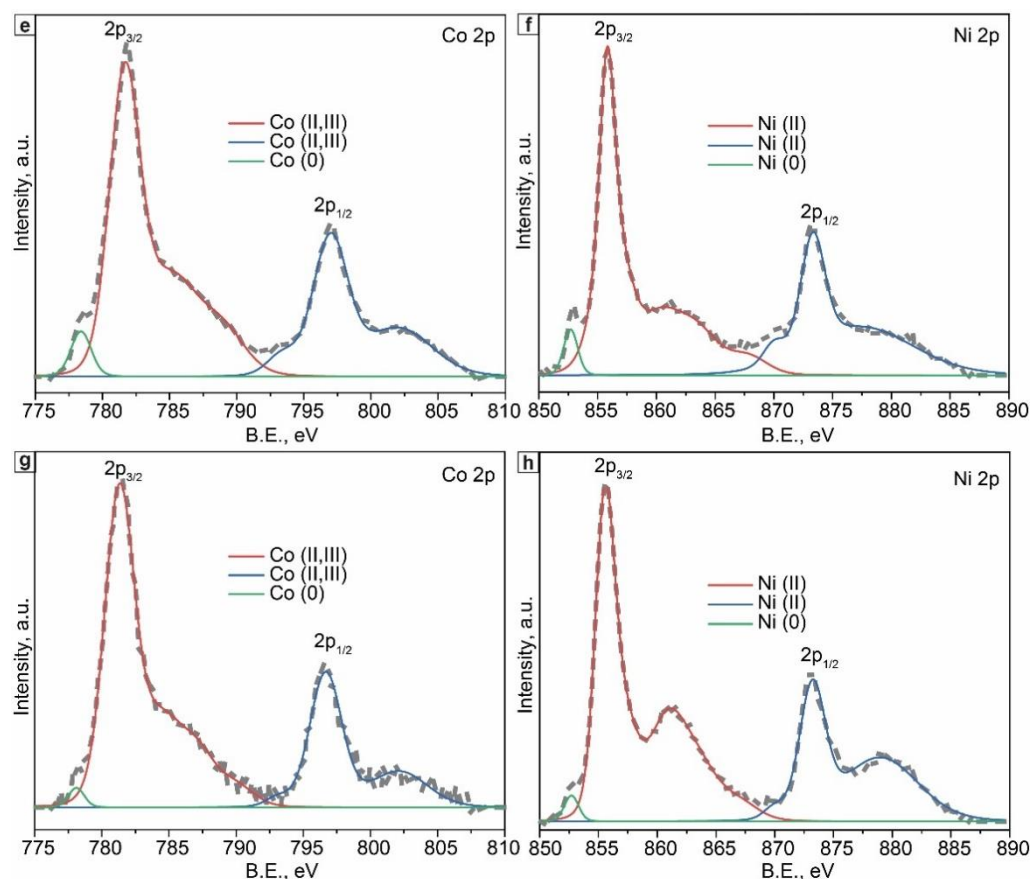
**Figure 3.** High-resolution XPS spectra of the as-synthesized (**a**) Co, (**b**) Ni, (**c,d**) $Co_3Ni$, (**e,f**) CoNi, and (**g,h**) $CoNi_3$ catalysts.

### 3.2. In Situ DRIFTS Experiments

Elicitation of the active sites for the analyzed single-phase and bimetallic catalysts was performed using DRIFTS-CO/$CO_2$ analysis. The similar behavior of all bands of the C-O stretching vibrations in the spectra of single Co and Ni catalysts did not allow the proper assignment of the bands in the spectra of the bimetallic samples (Figure S2). However, analysis of the DRIFT-CO spectra for single Co and Ni catalysts clearly elucidated (Figure S2) the presence of 2006, 2059, 2104, 2128, 2177 $cm^{-1}$, and 2010, 2056, 2114, 2166, 2222 $cm^{-1}$ bands, respectively. The presence of those bands identified few different Co and Ni electronic states, such as $Co^{2+}$-CO (2177 and 2128 $cm^{-1}$), $Co^{+}$-CO (2128 $cm^{-1}$), $Co^{\delta+}$-CO (2104 $cm^{-1}$), $Co^{0}$-CO (2059 and 2006 $cm^{-1}$) [2–16] and $Ni^{2+}$-CO (2222 and 2166 $cm^{-1}$), $Ni^{+}$-CO (2114 $cm^{-1}$), $Ni^{\delta+}$-CO (2056 $cm^{-1}$), and $Ni^{0}$-CO (2010 $cm^{-1}$) [2,3,17–25]. All of the data agreed well with the XPS results. The CO adsorption was fully reversible for the single-metal catalysts, and only a small amount of CO remained on the alloy catalyst surfaces after the finalizing vacuum treatment at room temperature.

In the case of the $CO_2$ adsorption on the catalysts with different Co and Ni compositions, a few weak spectra were observed in the 2400–2300 $cm^{-1}$ range of wavelengths (Figure 4). The corresponding bands were at 2338 $cm^{-1}$, 2345 $cm^{-1}$, 2339 $cm^{-1}$, 2345 $cm^{-1}$, and 2342 $cm^{-1}$ for the Co, Ni, $Co_3Ni$, CoNi, and $CoNi_3$ samples, respectively. These bands corresponded to the asymmetric valence $\upsilon_3$ vibrations of the adsorbed $CO_2$ molecules. The shift direction of these bands can be explained by the strong polarization of $CO_2$ molecules adsorbed on the alloy surfaces, which interacted with the cations [53].

In this study, the 2338 $cm^{-1}$ band was used as a standard; thus, a positive shift from 1 to 7 $cm^{-1}$ was observed for every sample except for the monometallic Co catalyst. These results indicate stronger adsorption of $CO_2$ molecules on the Ni, $Co_3Ni$, and $CoNi_3$ surfaces. The higher intensity of the lines in the Ni and $CoNi_3$ spectra indicated a larger number of

adsorbed $CO_2$ molecules on the surfaces of these samples. After the vacuum treatment at room temperature, the $CO_2$ spectra disappeared for the single-metal samples and are became less intense without any shift for the bimetallic CoNi and $CoNi_3$ samples, while a slight shift was observed for $Co_3Ni$ (Figure S3).
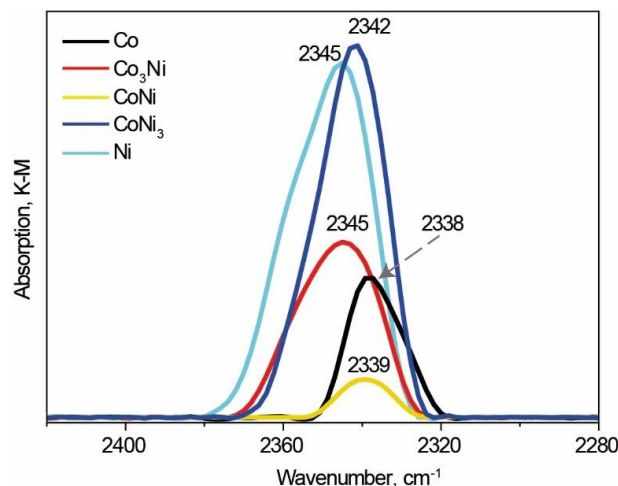


**Figure 4.** DRIFT-$CO_2$ spectra of Co, Ni, and bimetallic $Co_xNi_{1-x}$ catalysts.

### 3.3. Temperature-Programmed Reduction Experiments

$H_2$-TPR studies were performed to elucidate the surface reducibility of the prepared Co, $Co_3Ni$, CoNi, $CoNi_3$, and Ni catalysts (Figure 5). All TPR profiles are characterized by a wide range of $H_2$ consumption temperatures, which indicates the occurrence of several parallel reduction processes on the catalytic surface. The Co reduction profile exhibited two characteristic peaks at 269 °C and 390 °C. These results corresponded to the consistent reduction in Co oxides from $Co^{3+}$ to $Co^{2+}$ and from $Co^{2+}$ to $Co^0$ [54]. There were three peaks in the reduction profile of the Ni catalyst, with two of them in the 100–400 °C range, indicating desorption of C- and N-containing residuals, as well as chemisorbed water, which were detected by the XPS analysis. The third peak at 312 °C could be attributed to the reduction of $Ni^{2+}$ to Ni [55].
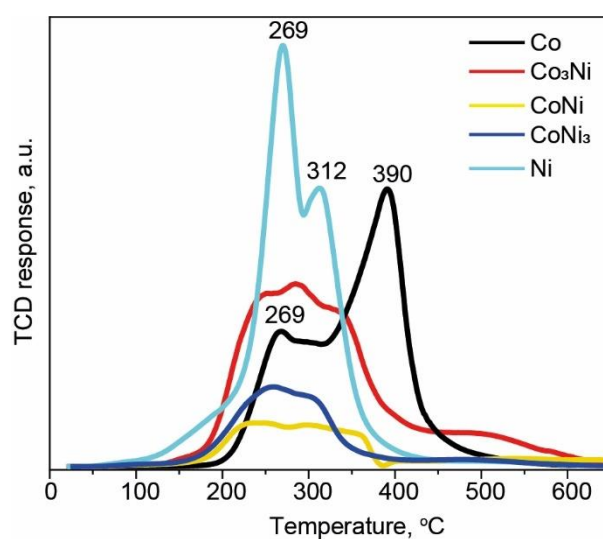


**Figure 5.** $H_2$-TPR profiles of Co, Ni, and bimetallic $Co_xNi_{1-x}$ catalysts.

All the bimetallic catalysts demonstrated lower $H_2$ consumption intensities, compared with the Co and Ni catalysts. These results suggest that the surfaces of the $Co_xNi_{1-x}$ alloys are less contaminated and more stable with respect to oxidation.

### 3.4. $CO_2$ Hydrogenation Performance

Catalytic activities of the as-synthesized Co, $Co_3Ni$, CoNi, $CoNi_3$, and Ni catalysts were evaluated for $CO_2$ hydrogenation at 300 °C. The experimental conditions at such temperature ensured the maximal thermodynamic conversion of $CO_2$ into $CH_4$. All the samples demonstrated exceptional selectivity with respect to the $CH_4$ formation, which was close to 100% (Table 2). Water was the main byproduct of the reaction, and only trace amounts of CO were detected.

**Table 2.** Catalytic performance of the $CO_2$ hydrogenation reaction, for the Co, $Co_3Ni$, CoNi, $CoNi_3$, and Ni catalysts (calculated at T = 300 °C, P = 2 MPa, $H_2:CO_2$ = 4:1, VHSV = 4500 mL·$g^{-1}h^{-1}$).

| Sample ID | $CH_4$ Selectivity, % | Efficiency by $CH_4$, mol·$h^{-1}$·$g_{cat}^{-1}$ | $CO_2$ Conversion, % |
|---|---|---|---|
| Co | 99+ | 0.12 | 71.5 |
| $Co_3Ni$ | 99+ | 0.21 | 89.1 |
| CoNi | 99+ | 0.24 | 88.4 |
| $CoNi_3$ | 99+ | 0.27 | 88.7 |
| Ni | 99+ | 0.09 | 66.6 |

The Co catalyst exhibited a slightly higher efficiency with respect to the $CH_4$ formation calculated per gram (0.12 mol·$h^{-1}$·$g_{cat}^{-1}$) of the active component, compared with the Ni catalyst (0.09 mol·$h^{-1}$·$g_{cat}^{-1}$). Nevertheless, bimetallic $Co_xNi_{1-x}$ alloy-based catalysts exhibited twofold to threefold higher activity, where the $CoNi_3$ was the most active composition (0.27 mol·$h^{-1}$·$g_{cat}^{-1}$). The values for the $CH_4$ efficiency formation over the bimetallic catalysts were similar, but they tended to increase with increasing the Ni content (Table 2). The $CO_2$ conversion observed for the alloy catalysts was approximately 89%, much higher than for pure metals, that is, 67% and 72% for Ni and Co, respectively.

### 3.5. Catalyst Stability and Productivity Test

$CoNi_3$ and CoNi alloys with the highest catalytic activity were further used for assessing the stability of bimetallic bulk catalysts compared with the Ni catalyst, which is considered to be one of the basic components for producing synthetic natural gas by the hydrogenation of $CO_2$. Figure 6 shows the activity and selectivity of the $CO_2$ hydrogenation reaction with respect to $CH_4$, over the 80-h-long TOS at 300 °C. The samples reached maximal catalytic activity after 6 h from the beginning of the experiment (Figure 6a). The Ni catalyst began to lose its activity monotonously throughout the reaction. The maximal decrease was 53% at 80 h of TOS. Simultaneously, the selectivity of $CH_4$ dropped to 76%, and the CO fraction became more visible.
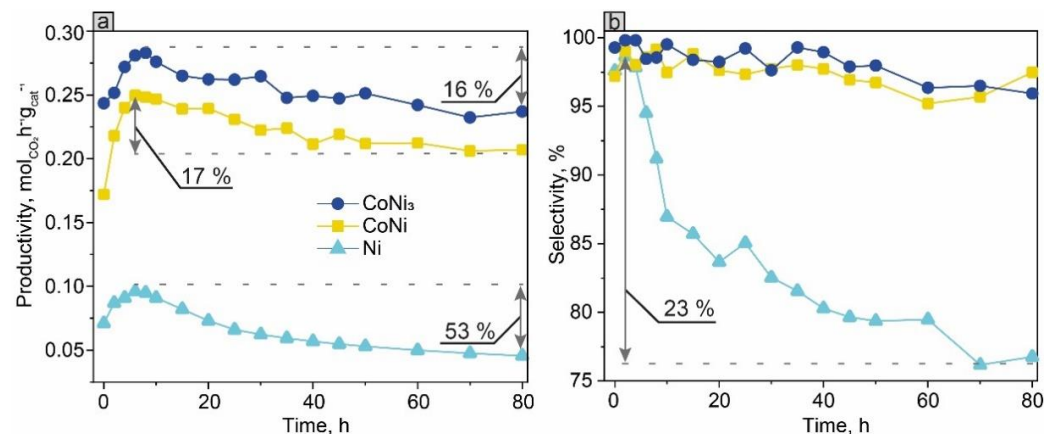


**Figure 6.** Productivity (**a**) and $CH_4$ selectivity (**b**) for the CoNi, $CoNi_3$, and Ni catalysts, during the 80-h-long $CO_2$ hydrogenation reaction at 300 °C.

Evidently, alloy-based catalysts exhibited much better stability. After 80 h of TOS, the catalytic activity dropped only by ~16% both for the CoNi and CoNi$_3$ alloys. It is worth noting that a slight decrease in activity (by 15–20%) during the first hours of the run is expected for activated catalysts [56]. At the same time, the extremely high selectivity (>99%) with respect to the CH$_4$ formation remained constant throughout the experiment, indicating the stability of the catalytic properties of the active sites.

## 4. Discussion

### 4.1. CO$_2$ Hydrogenation Performance

All of the above-discussed bimetallic bulk catalysts exhibited high catalytic activity with respect to the CO$_2$ hydrogenation reaction, comparable to the most effective reported catalysts [29]. However, most of the reported results are related to supported catalysts. In addition, for supported monometallic catalysts, Ni is typically more active than Co [57]. In our case, the bulk monometallic Co catalyst prepared by combustion was more active than the Ni-based catalyst. This conclusion is in agreement with the DRIFT data (Figure 4), where a stronger adsorption of CO$_2$ was observed on the Ni surface than on the Co bulk catalyst. Moreover, the porosity of the Co catalyst was significantly higher than that of Ni (Figure 2), which might have reduced the diffusion constraint. Such a result shows that the dependence of the catalytic activity on the nature of the active metal is not straightforward, as is commonly believed. The mechanism of the CO$_2$ transformation depends on the supporting material [57–59] and can be affected by the morphology of the catalytic constituents.

A more important observation was that a combination of Co and Ni constituents led to a synergistic effect with respect to the catalytic activity of bulk alloy catalysts. Bulk alloy catalysts exhibited twofold to threefold higher activities than monometallic SGCS catalysts (Table 2). The crystallite size of the SGCS catalysts was approximately 30–40 nm (Table 1), higher than that of the supported analogues (5–10 nm) [60]. Hence, based on the commonly used paradigm, the catalytic activity of bulk Co-Ni materials should be much lower than that of supported materials. Nevertheless, the activity of the SGCS Co$_x$Ni$_{1-x}$ catalysts was comparable to or even higher than that of many reported supported catalysts. The active phase content of supported Ni/Co-based catalysts usually does not exceed 20 wt % [29,61], which is close to that used in this work. However, in the case of the SGCS sponge-like catalysts, the catalytically active surface was potentially equivalent to the overall surface of the 100 μm diameter metallic sponge-like particles.

In addition, comparing the results of the long-term tests, it can be concluded that the introduction of Co stabilized the catalyst properties, protecting it from deactivation (Figure 6). The XPS results showed that before the catalysis, the Co concentration on the outermost surface of the SGCS alloy catalysts was higher than that of Ni, even when the stoichiometric ratio of the constituents was kept in a larger volume. A similar trend has been observed in other studies [42]. However, after the catalysis, the amount of Ni on the surface increased (Table S1). Thus, it may be suggested that owing to the higher affinity for O, Co protected the Ni active sites from oxidation during the reaction (see also [48]). The H$_2$-TPR results support this conclusion, showing the better oxidation resistance of the alloys relative to pure Ni (Figure 5).

In addition, the majority of publications on CO$_2$ hydrogenation outline the problem of the low thermal stability of the catalysts and their fast deactivation [59]. The application of catalytically active elements on the surface of an inert supporting material is usually considered a universal solution of this problem. This tendency has historical roots when the approach is used to optimize catalysts based on noble metals [62]. Still, in the case of the CO$_2$ hydrogenation on the Ni-supported catalyst, significant difference between the thermal conductivities of Ni (90.7 W/m·K) and ceramic supports (e.g., CeO$_2$ at 8 W/m·K [28]) could yield local hot spots and subsequent carbonization of active sites [11,29]. In this work, active sites were distributed on relatively large (100–500 μm) metallic particles, which provided additional space and time for extensive heat dissipation. Moreover, the unique

morphology of these particles generated during combustion synthesis manifested as a highly porous sponge structure and an additional instrument for fast heat and mass transfer. These features positively affected the stability of the SGCS catalysts.

Thus, it can be concluded that the catalytic efficiency of one active metal can be significantly enhanced by the addition of another active metal. More importantly, alloys show much higher stability than pure catalysts. Indeed, the bulk Ni catalyst prepared using an energy-saving combustion approach was stabilized by the addition of another catalytically active metal such as Co. In addition, it is important to note that typical oxide-based supports stabilize the metal oxide phase, leading to a high reduction temperature [63]. For example, industrial activation of Ni-based catalysts occurs at 400 °C, while the reduction process of the catalysts synthesized in this work already ended at 350 °C (Figure 5). Thus, the implementation of the SGCS bulk alloy catalysts might be a step toward the simplification of the catalyst production approach and the higher cost efficiency of the $CO_2$ hydrogenation reaction. However, to control the process, it is critical to understand the hydrogenation mechanism associated with the catalysts used.

### 4.2. Comments on the Possible $CO_2$ Hydrogenation Mechanism

The $CoNi_3$ catalyst was chosen as the most active catalyst for investigating the $CO_2$ hydrogenation reaction mechanism. The presence of $CH_4$ and CO as the main reaction products suggests two viable reaction paths: the formation of $CH_4$ through the CO intermediate (overall sequence of Reactions (6) and (7)) or directly from $CO_2$ (overall Reaction (8)):

$$CO_2 + H_2 \rightarrow CO + H_2O \tag{6}$$

$$CO + 3H_2 \rightarrow CH_4 + H_2O \tag{7}$$

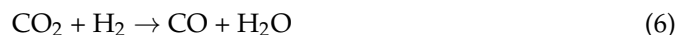$$CO_2 + 4H_2 \rightarrow CH_4 + 2H_2O \tag{8}$$

Figure 7 shows the selectivity ratio of hydrocarbons to CO formation as a function of the contact time of the feeding mixture with the $CoNi_3$ catalyst. It can be clearly observed that at a lower contact time, the S(HC)/S(CO) ratio tends to zero. This observation suggests that in our case, CO formed first (Reaction (6)) and later transformed to $CH_4$ (Reaction (7)).
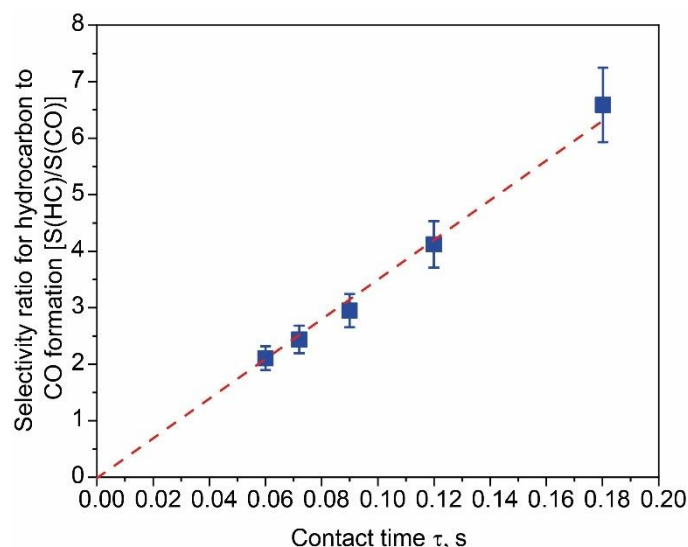


**Figure 7.** The ratio between HC and CO selectivity as a function of the contact time.

The dependence of the concentration of gaseous precursors and products on contact time is shown in Figure 8. The concentration of the feeding gas reagents decreases with time, while the concentrations of $CH_4$ and $H_2O$ products constantly increase. The value of the CO gas concentration reaches a maximum and then decreases toward zero. This

behavior is characteristic of the final product formation through consecutive reactions. Thus, we hypothesize that the formation of $CH_4$ from $CO_2$ involves an intermediate stage of the CO formation. It should be noted that even at its peak, the CO concentration was twice lower that of the $CH_4$ concentration. This means that the reaction rate of the CO formation was significantly lower than that of the $CH_4$ formation. Thus, the CO formation reaction is the limiting stage of the overall process.
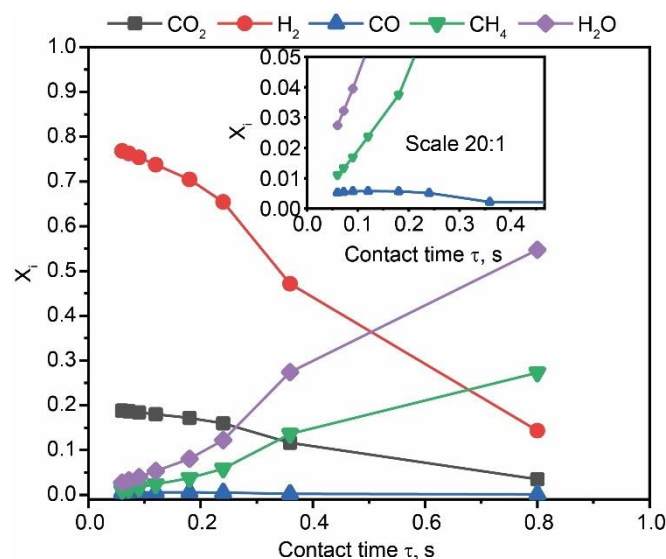


**Figure 8.** Dependence of the concentration of precursors and products as a function of the contact time.

Finally, it has been reported that the distinctive feature of Co, compared with Ni, is its ability to catalyze not only direct $CO_2$ methanation but also the reverse water shift reaction, with the formation of CO [58,64]. Therefore, it is possible that the presence of Co enhances the rate of the CO gas formation, which is later converted to $CH_4$. Moreover, according to the DRIFT-$CO_2$ analysis, the presence of Co decreases $CO_2$ adsorption on the surface of the alloy and thus protects the Ni active sites from poisoning through the formation of solid C layers, which blocks the access of the feeding gas to the Ni active sites.

## 5. Conclusions

In this study, bulk single-phase Co-Ni alloy catalysts with broad $Co_xNi_{1-x}$ composition (x = 1, 0.75, 0.5, 0.25, and 0) were synthesized by the combustion of reactive sol-gels. The catalysts had a sponge-like microstructure and a highly crystallized intermetallic FCC crystal structure. The overall desired stoichiometric Co/Ni ratio was well-preserved in the volume of the materials, while the near surface of the $Co_xNi_{1-x}$ alloys saturated twice with Co. Gradual addition of Co into Ni allowed the governing of the alloy microstructure and obtaining a more porous structure and a smaller intermetallic crystallite size.

The combination of Co and Ni in a single phase resulted in a synergistic effect with respect to the catalytic activity, showing threefold higher efficiency than that of single-metal catalysts. The $CoNi_3$ composition was the most active catalyst with efficiency to the $CH_4$ formation of 0.27 mol·h$^{-1}$·g$_{cat}$$^{-1}$ at VHSV = 4500 mL·g$^{-1}$h$^{-1}$. It was also demonstrated that the Co constituent stabilized the catalyst toward deactivation. At the same time, the selectivity for 99+% methane formation on the alloy samples remained constant throughout the experiment. Moreover, the bimetallic catalysts demonstrated lower $H_2$ consumption intensity than the monometallic catalysts, indicating that the alloys are more stable to oxidation.

A study of the relationship between the concentration of both the feeding mixture and gaseous products on the catalyst surfaces during the hydrogenation process allows us to suggest the $CO_2$ hydrogenation mechanism. This implies that the overall hydrogenation

proceeds in a sequence of steps. First, the Co active sites facilitate the formation of gaseous CO, followed by its conversion to $CH_4$. Moreover, the presence of Co decreases the $CO_2$ adsorption on the $Co_xN_{1-x}$ surface and hence protects the Ni active sites from oxidation and formation of solid C particles, i.e., poisoning of the catalyst.

The fact that the activity of SGCS $Co_xNi_{1-x}$ catalysts is comparable or even higher than that of supported catalysts suggests that the implementation of bulk sponge-like porous alloys can be a step toward simplification of catalyst production technology and the development of an efficient approach to handle the problem of $CO_2$ emission into the atmosphere.

**Supplementary Materials:** The following supporting information can be downloaded at https://www.mdpi.com/article/10.3390/ma15155129/s1: Figure S1: EDS spectra of $Co_3Ni$ (a), CoNi (b), and $CoNi_3$ (c) catalysts; Table S1: XPS average elements content in the outermost surface of the Co-Ni catalysts; Figure S2: DRIFT-CO spectra of single Co, Ni, and bimetallic $Co_xNi_{1-x}$ catalysts; Figure S3: DRIFT-$CO_2$ absorption-desorption spectra of Co (a), Ni (b), $Co_3Ni$ (c), CoNi (d), and $CoNi_3$ (e).

**Conflicts of Interest:** The authors declare no conflict of interest.

# References

1. Lee, W.J.; Li, C.; Prajitno, H.; Yoo, J.; Patel, J.; Yang, Y.; Lim, S. Recent Trend in Thermal Catalytic Low Temperature $CO_2$ Methanation: A Critical Review. *Catal. Today* **2021**, *368*, 2–19. [CrossRef]
2. Takht Ravanchi, M.; Sahebdelfar, S. Catalytic Conversions of $CO_2$ to Help Mitigate Climate Change: Recent Process Developments. *Process Saf. Environ. Prot.* **2021**, *145*, 172–194. [CrossRef]
3. Li, Y.; Chan, S.H.; Sun, Q. Heterogeneous Catalytic Conversion of $CO_2$: A Comprehensive Theoretical Review. *Nanoscale* **2015**, *7*, 8663–8683. [CrossRef]
4. Modak, A.; Bhanja, P.; Dutta, S.; Chowdhury, B.; Bhaumik, A. Catalytic Reduction of $CO_2$into Fuels and Fine Chemicals. *Green Chem.* **2020**, *22*, 4002–4033. [CrossRef]
5. Porosoff, M.D.; Yan, B.; Chen, J.G. Catalytic Reduction of $CO_2$ by H2 for Synthesis of CO, Methanol and Hydrocarbons: Challenges and Opportunities. *Energy Environ. Sci.* **2016**, *9*, 62–73. [CrossRef]
6. Zhang, T.; Zhong, J.; Wu, Z. Recent Advances in Catalytic Conversion of Carbon Dioxide to Propiolic Acids over Coinage-Metal-Based Catalysts. *J. Energy Chem.* **2021**, *59*, 572–580. [CrossRef]
7. Sreedhar, I.; Varun, Y.; Singh, S.A.; Venugopal, A.; Reddy, B.M. Developmental Trends in $CO_2$ Methanation Using Various Catalysts. *Catal. Sci. Technol.* **2019**, *9*, 4478–4504. [CrossRef]
8. Fan, W.K.; Tahir, M. Recent Trends in Developments of Active Metals and Heterogenous Materials for Catalytic $CO_2$hydrogenation to Renewable Methane: A Review. *J. Environ. Chem. Eng.* **2021**, *9*, 105460. [CrossRef]
9. Panagiotopoulou, P. Hydrogenation of $CO_2$ over Supported Noble Metal Catalysts. *Appl. Catal. A Gen.* **2017**, *542*, 63–70. [CrossRef]
10. Price, C.A.H.; Reina, T.R.; Liu, J. Engineering Heterogenous Catalysts for Chemical $CO_2$ Utilization: Lessons from Thermal Catalysis and Advantages of Yolk@shell Structured Nanoreactors. *J. Energy Chem.* **2021**, *57*, 304–324. [CrossRef]
11. Lv, C.; Xu, L.; Chen, M.; Cui, Y.; Wen, X.; Li, Y.; Wu, C.E.; Yang, B.; Miao, Z.; Hu, X.; et al. Recent Progresses in Constructing the Highly Efficient Ni Based Catalysts with Advanced Low-Temperature Activity Toward $CO_2$ Methanation. *Front. Chem.* **2020**, *8*, 269. [CrossRef] [PubMed]
12. Gac, W.; Zawadzki, W.; Rotko, M.; Greluk, M.; Słowik, G.; Kolb, G. Effects of Support Composition on the Performance of Nickel Catalysts in $CO_2$ Methanation Reaction. *Catal. Today* **2020**, *357*, 468–482. [CrossRef]
13. Schreiter, N.; Kirchner, J.; Kureti, S. A DRIFTS and TPD Study on the Methanation of $CO_2$ on $Ni/Al_2O_3$ Catalyst. *Catal. Commun.* **2020**, *140*, 105988. [CrossRef]
14. Messou, D.; Bernardin, V.; Meunier, F.; Ordoño, M.B.; Urakawa, A.; Machado, B.F.; Collière, V.; Philippe, R.; Serp, P.; Le Berre, C. Origin of the Synergistic Effect between $TiO_2$ Crystalline Phases in the $Ni/TiO_2$-Catalyzed $CO_2$ Methanation Reaction. *J. Catal.* **2021**, *398*, 14–28. [CrossRef]

15. Zhou, R.; Rui, N.; Fan, Z.; Liu, C. jun Effect of the Structure of Ni/TiO$_2$ Catalyst on CO$_2$ Methanation. *Int. J. Hydrogen Energy* **2016**, *41*, 22017–22025. [CrossRef]

16. Ye, R.P.; Gong, W.; Sun, Z.; Sheng, Q.; Shi, X.; Wang, T.; Yao, Y.; Razink, J.J.; Lin, L.; Zhou, Z.; et al. Enhanced Stability of Ni/SiO$_2$ Catalyst for CO$_2$ Methanation: Derived from Nickel Phyllosilicate with Strong Metal-Support Interactions. *Energy* **2019**, *188*, 116059. [CrossRef]

17. Zhang, X.; Sun, W.J.; Chu, W. Effect of Glow Discharge Plasma Treatment on the Performance of Ni/SiO$_2$ Catalyst in CO$_2$ Methanation. *Ranliao Huaxue Xuebao J. Fuel Chem. Technol.* **2013**, *41*, 96–101. [CrossRef]

18. Pu, T.; Shen, L.; Liu, X.; Cao, X.; Xu, J.; Wachs, I.E.; Zhu, M. Formation and Influence of Surface Hydroxyls on Product Selectivity during CO$_2$ Hydrogenation by Ni/SiO$_2$ Catalysts. *J. Catal.* **2021**, *400*, 228–233. [CrossRef]

19. Bian, Z.; Chan, Y.M.; Yu, Y.; Kawi, S. Morphology Dependence of Catalytic Properties of Ni/CeO$_2$ for CO$_2$ Methanation: A Kinetic and Mechanism Study. *Catal. Today* **2020**, *347*, 31–38. [CrossRef]

20. Tada, S.; Shimizu, T.; Kameyama, H.; Haneda, T.; Kikuchi, R. Ni/CeO$_2$ Catalysts with High CO$_2$ Methanation Activity and High CH4 Selectivity at Low Temperatures. *Int. J. Hydrog. Energy* **2012**, *37*, 5527–5531. [CrossRef]

21. Hu, L.; Urakawa, A. Continuous CO$_2$ Capture and Reduction in One Process: CO$_2$ Methanation over Unpromoted and Promoted Ni/ZrO$_2$. *J. CO$_2$ Util.* **2018**, *25*, 323–329. [CrossRef]

22. Ilsemann, J.; Sonström, A.; Gesing, T.M.; Anwander, R.; Bäumer, M. Highly Active Sm$_2$O$_3$ -Ni Xerogel Catalysts for CO$_2$ Methanation. *ChemCatChem* **2019**, *11*, 1732–1741. [CrossRef]

23. Siakavelas, G.I.; Charisiou, N.D.; AlKhoori, A.; AlKhoori, S.; Sebastian, V.; Hinder, S.J.; Baker, M.A.; Yentekakis, I.V.; Polychronopoulou, K.; Goula, M.A. Highly Selective and Stable Ni/La-M (M=Sm, Pr, and Mg)-CeO$_2$ Catalysts for CO$_2$ Methanation. *J. CO$_2$ Util.* **2021**, *51*, 101618. [CrossRef]

24. Gholami, S.; Alavi, S.M.; Rezaei, M. CO$_2$ Methanation over Nanocrystalline Ni Catalysts Supported on Mechanochemically Synthesized Cr$_2$O$_3$-M (M=Fe, Co, La, and Mn) Carriers. *Int. J. Hydrog. Energy* **2021**, *46*, 35571–35584. [CrossRef]

25. Grad, O.; Mihet, M.; Blanita, G.; Dan, M.; Barbu-Tudoran, L.; Lazar, M.D. MIL-101-Al$_2$O$_3$ as Catalytic Support in the Methanation of CO$_2$–Comparative Study between Ni/MIL-101 and Ni/MIL-101-Al$_2$O$_3$ Catalysts. *Catal. Today* **2021**, *366*, 114–122. [CrossRef]

26. Daroughegi, R.; Meshkani, F.; Rezaei, M. Enhanced Low-Temperature Activity of CO$_2$ Methanation over Ceria-Promoted Ni-Al$_2$O$_3$ Nanocatalyst. *Chem. Eng. Sci.* **2021**, *230*, 116194. [CrossRef]

27. Li, S.; Liu, G.; Zhang, S.; An, K.; Ma, Z.; Wang, L.; Liu, Y. Cerium-Modified Ni-La$_2$O$_3$/ZrO$_2$ for CO$_2$ Methanation. *J. Energy Chem.* **2020**, *43*, 155–164. [CrossRef]

28. Malakkal, L.; Prasad, A.; Oladimeji, D.; Jossou, E.; Ranasinghe, J. Atomistic and Experimental Study on Thermal Conductivity of Bulk and Porous Cerium Dioxide. *Sci. Rep.* **2019**, *9*, 6326. [CrossRef]

29. Zhao, B.; Liu, P.; Li, S.; Shi, H.; Jia, X.; Wang, Q.; Yang, F.; Song, Z.; Guo, C.; Hu, J.; et al. Bimetallic Ni-Co Nanoparticles on SiO$_2$ as Robust Catalyst for CO Methanation: Effect of Homogeneity of Ni-Co Alloy. *Appl. Catal. B Environ.* **2020**, *278*, 119307. [CrossRef]

30. Tsiotsias, A.I.; Charisiou, N.D.; Yentekakis, I.V.; Goula, M.A. Bimetallic Ni-Based Catalysts for Co2 Methanation: A Review. *Nanomaterials* **2021**, *11*, 28. [CrossRef]

31. Alrafei, B.; Polaert, I.; Ledoux, A.; Azzolina-Jury, F. Remarkably Stable and Efficient Ni and Ni-Co Catalysts for CO$_2$ Methanation. *Catal. Today* **2020**, *346*, 23–33. [CrossRef]

32. Koh, A.C.W.; Chen, L.; Kee Leong, W.; Johnson, B.F.G.; Khimyak, T.; Lin, J. Hydrogen or Synthesis Gas Production via the Partial Oxidation of Methane over Supported Nickel-Cobalt Catalysts. *Int. J. Hydrog. Energy* **2007**, *32*, 725–730. [CrossRef]

33. González-Castaño, M.; Navarro de Miguel, J.C.; Boelte, J.H.; Centeno, M.A.; Klepel, O.; Arellano-García, H. Assessing the Impact of Textural Properties in Ni–Fe Catalysts for CO$_2$ Methanation Performance. *Microporous Mesoporous Mater.* **2021**, *327*, 111405. [CrossRef]

34. Jia, X.; Zhang, X.; Rui, N.; Hu, X.; Liu, C. jun Structural Effect of Ni/ZrO$_2$ Catalyst on CO$_2$ Methanation with Enhanced Activity. *Appl. Catal. B Environ.* **2019**, *244*, 159–169. [CrossRef]

35. García-Moncada, N.; Navarro, J.C.; Odriozola, J.A.; Lefferts, L.; Faria, J.A. Enhanced Catalytic Activity and Stability of Nanoshaped Ni/CeO$_2$ for CO$_2$ Methanation in Micro-Monoliths. *Catal. Today* **2022**, *383*, 205–215. [CrossRef]

36. Ye, R.P.; Li, Q.; Gong, W.; Wang, T.; Razink, J.J.; Lin, L.; Qin, Y.Y.; Zhou, Z.; Adidharma, H.; Tang, J.; et al. High-Performance of Nanostructured Ni/CeO$_2$ Catalyst on CO$_2$ Methanation. *Appl. Catal. B Environ.* **2020**, *268*, 118474. [CrossRef]

37. Wang, L.; Hu, J.; Liu, H.; Wei, Q.; Gong, D.; Mo, L.; Tao, H.; Zhang, C. Three-Dimensional Mesoporous Ni-CeO$_2$ Catalysts with Ni Embedded in the Pore Walls for Co2 Methanation. *Catalysts* **2020**, *10*, 523. [CrossRef]

38. Lan, H.; Mekonnen, W.; Shen, Q.; Yu, Z. Bed Packing Configuration and Hot-Spot Utilization for Low-Temperature CO$_2$ Methanation on Monolithic Reactor. *Chem. Eng. J.* **2022**, *428*, 131106. [CrossRef]

39. Zhang, R.; Chen, H.; Mu, Y.; Chansai, S.; Ou, X.; Hardacre, C.; Jiao, Y.; Fan, X. Structured Ni @ NaA Zeolite Supported on Silicon Carbide Foam Catalysts for Catalytic Carbon Dioxide Methanation. *AIChE J.* **2020**, *66*, 1538–1549. [CrossRef]

40. Frey, M.; David, E. Optimization of Structured Cellular Foam-Based Catalysts for Low-Temperature Carbon Dioxide Methanation in a Platelet. *Comptes Rendus Chim.* **2015**, *18*, 283–292. [CrossRef]

41. Kang, C.; Liejin, G.U.O.; Hui, W. A Review on Thermal Application of Metal Foam. *Sci. China Technol. Sci.* **2020**, *63*, 2469–2490. [CrossRef]

42. Khort, A.; Hedberg, J.; Mei, N.; Romanovski, V.; Blomberg, E.; Odnevall, I. Corrosion and Transformation of Solution Combustion Synthesized Co, Ni and CoNi Nanoparticles in Synthetic Freshwater with and without Natural Organic Matter. *Sci. Rep.* **2021**, *11*, 7860. [CrossRef] [PubMed]

43. Sdobnyakov, N.; Khort, A.; Myasnichenko, V.; Podbolotov, K.; Romanovskaia, E.; Kolosov, A.; Sokolov, D.; Romanovski, V. Solution Combustion Synthesis and Monte Carlo Simulation of the Formation of CuNi Integrated Nanoparticles. *Comput. Mater. Sci.* **2020**, *184*, 109936. [CrossRef]

44. Khort, A.; Roslyakov, S.; Loginov, P. Solution Combustion Synthesis of Single-Phase Bimetallic Nanomaterials. *Nano Struct. Nano Objects* **2021**, *26*, 100727. [CrossRef]

45. Yermekova, Z.; Roslyakov, S.I.; Kovalev, D.Y.; Danghyan, V.; Mukasyan, A.S. One-Step Synthesis of Pure γ-FeNi Alloy by Reactive Sol-Gel Combustion Route Mechanism and Properties. *J. Sol Gel Sci. Technol.* **2020**, *94*, 310–321. [CrossRef]

46. Roslyakov, S.; Yermekova, Z.; Trusov, G.; Khort, A.; Evdokimenko, N.; Bindiug, D.; Karpenkov, D.; Zhukovskyi, M.; Degtyarenko, A.; Mukasyan, A. One-Step Solution Combustion Synthesis of Nanostructured Transition Metal Antiperovskite Nitride and Alloy. *Nano Struct. Nano Objects* **2021**, *28*, 100796. [CrossRef]

47. Kustov, L.M. New Trends in IR-Spectroscopic Characterization of Acid and Basic Sites in Zeolites and Oxide Catalysts. *Top. Catal.* **1997**, *4*, 131–144. [CrossRef]

48. Shpiro, E.S.; Rudnyi, Y.; Tkachenko, O.P.; Antoshin, G.V.; Dyusenbina, B.B.; Minachev, K.M. Surface Compositions of Co-Ni Alloys and the Action of These Alloys as Sorbents for Nitrogen and Carbon Monoxide. *Bull. Acad. Sci. USSR Div. Chem. Sci.* **1981**, *30*, 2036–2040. [CrossRef]

49. Denton, A.R.; Ashcroft, N.W. Vegards Law. *Phys. Rev. A* **1991**, *43*, 3161–3164. [CrossRef]

50. Xu, L.; Lian, X.; Chen, M.; Cui, Y.; Wang, F.; Li, W.; Huang, B. $CO_2$ Methanation over Co–Ni Bimetal-Doped Ordered Mesoporous $Al_2O_3$ Catalysts with Enhanced Low-Temperature Activities. *Int. J. Hydrog. Energy* **2018**, *43*, 30750–30759. [CrossRef]

51. Liu, Q.; Bian, B.; Fan, J.; Yang, J. Cobalt Doped Ni Based Ordered Mesoporous Catalysts for $CO_2$ Methanation with Enhanced Catalytic Performance. *Int. J. Hydrog. Energy* **2018**, *43*, 4893–4901. [CrossRef]

52. Fatah, N.A.A.; Jalil, A.A.; Salleh, N.F.M.; Hamid, M.Y.S.; Hassan, Z.H.; Nawawi, M.G.M. Elucidation of Cobalt Disturbance on $Ni/Al_2O_3$ in Dissociating Hydrogen towards Improved $CO_2$ Methanation and Optimization by Response Surface Methodology (RSM). *Int. J. Hydrog. Energy* **2020**, *45*, 18562–18573. [CrossRef]

53. Ward, J.W.; Habgood, H.W. The Infrared Spectra of Carbon Dioxide Adsorbed on Zeolite X. *J. Phys. Chem.* **1966**, *70*, 1178–1182. [CrossRef]

54. Gou, Y.; Liang, X.; Chen, B. Porous Ni-Co Bimetal Oxides Nanosheets and Catalytic Properties for CO Oxidation. *J. Alloys Compd.* **2013**, *574*, 181–187. [CrossRef]

55. Lim, T.H.; Cho, S.J.; Yang, H.S.; Engelhard, M.H.; Kim, D.H. Effect of Co/Ni Ratios in Cobalt Nickel Mixed Oxide Catalysts on Methane Combustion. *Appl. Catal. A Gen.* **2015**, *505*, 62–69. [CrossRef]

56. Rivero-Mendoza, D.E.; Stanley, J.N.G.; Scott, J.; Aguey-Zinsou, K.F. An Alumina-Supported Ni-La-Based Catalyst for Producing Synthetic Natural Gas. *Catalysts* **2016**, *6*, 170. [CrossRef]

57. Bradford, M.C.J.; Vannice, M.A. $CO_2$ Reforming of $CH_4$. *Catal. Rev. Sci. Eng.* **1999**, *41*, 1–42. [CrossRef]

58. Wang, W.; Wang, S.; Ma, X.; Gong, J. Recent Advances in Catalytic Hydrogenation of Carbon Dioxide. *Chem. Soc. Rev.* **2011**, *40*, 3703–3727. [CrossRef]

59. Kirchner, J.; Baysal, Z.; Kureti, S. Activity and Structural Changes of Fe-Based Catalysts during $CO_2$ Hydrogenation towards $CH_4$–A Mini Review. *ChemCatChem* **2020**, *12*, 981–988. [CrossRef]

60. Jin, R. The Impacts of Nanotechnology on Catalysis by Precious Metal Nanoparticles. *Nanotechnol. Rev.* **2012**, *1*, 31–56. [CrossRef]

61. Guo, L.; Sun, J.; Ge, Q.; Tsubaki, N. Recent Advances in Direct Catalytic Hydrogenation of Carbon Dioxide to Valuable C2+ Hydrocarbons. *J. Mater. Chem. A* **2018**, *6*, 23244–23262. [CrossRef]

62. Ahmadi, M.; Mistry, H.; Roldan Cuenya, B. Tailoring the Catalytic Properties of Metal Nanoparticles via Support Interactions. *J. Phys. Chem. Lett.* **2016**, *7*, 3519–3533. [CrossRef] [PubMed]

63. Cuenya, B.R. Synthesis and Catalytic Properties of Metal Nanoparticles: Size, Shape, Support, Composition, and Oxidation State Effects. *Thin Solid Films* **2010**, *518*, 3127–3150. [CrossRef]

64. Saeidi, S.; Najari, S.; Fazlollahi, F.; Nikoo, M.K.; Sefidkon, F.; Klemeš, J.J.; Baxter, L.L. Mechanisms and Kinetics of $CO_2$ Hydrogenation to Value-Added Products: A Detailed Review on Current Status and Future Trends. *Renew. Sustain. Energy Rev.* **2017**, *80*, 1292–1311. [CrossRef]